The 60 pc Environment of FRB 20180916B

Shriharsh P. Tendulkar[1,2] , Armando Gil de Paz[3,4] , Aida Yu. Kirichenko[5,6] , Jason W. T. Hessels[7,8] , Mohit Bhardwaj[9,10] ,
Fernando Ávila[11], Cees Bassa[8] , Pragya Chawla[9,10] , Emmanuel Fonseca[9,10,12,13] , Victoria M. Kaspi[9,10] ,
Aard Keimpema[14] , Franz Kirsten[15] , T. Joseph W. Lazio[16], Benito Marcote[14] , Kiyoshi Masui[17,18] , Kenzie Nimmo[7,8] ,
Zsolt Paragi[14] , Mubdi Rahman[19,20] , Daniel Reverte Payá[21,22] , Paul Scholz[19] , and Ingrid Stairs[23]

[1] Department of Astronomy and Astrophysics, Tata Institute of Fundamental Research, Homi Bhabha Road, Colaba, Mumbai, Maharashtra, 400005, India
shriharsh.tendulkar@tifr.res.in
[2] National Centre for Radio Astrophysics, Pune University Campus, Post Bag 3, Ganeshkhind, Pune, 411007, India
[3] Departamento de Física de la Tierra y Astrofísica, Universidad Complutense de Madrid (UCM), Plaza Ciencias 1, Madrid, E-28040, Spain
[4] Instituto de Física de Partículas y del Cosmos (IPARCOS), Plaza Ciencias 1, Madrid, E-28040, Spain
[5] Instituto de Astronomía, Universidad Nacional Autónoma de México, Apdo. Postal 877, Ensenada, Baja California 22800, Mexico
[6] Ioffe Institute, 26 Politekhnicheskaya st., St. Petersburg 194021, Russia
[7] Anton Pannekoek Institute for Astronomy, University of Amsterdam, Science Park 904, 1098 XH, Amsterdam, The Netherlands
[8] ASTRON, Netherlands Institute for Radio Astronomy, Oude Hoogeveensedijk 4, 7991 PD Dwingeloo, The Netherlands
[9] Department of Physics, McGill University, 3600 rue University, Montréal, QC H3A 2T8, Canada
[10] McGill Space Institute, McGill University, 3550 rue University, Montréal, QC H3A 2A7, Canada
[11] Observatorio Astronómico Nacional, Instituto de Astronomía, Universidad Nacional Autónoma de México, Ensenada, Baja California, Mexico
[12] Department of Physics and Astronomy, West Virginia University, P.O. Box 6315, Morgantown, WV 26506, USA
[13] Center for Gravitational Waves and Cosmology, West Virginia University, Chestnut Ridge Research Building, Morgantown, WV 26505, USA
[14] Joint Institute for VLBI ERIC, Oude Hoogeveensedijk 4, 7991 PD Dwingeloo, The Netherlands
[15] Department of Space, Earth and Environment, Chalmers University of Technology, Onsala Space Observatory, SE-439 92, Onsala, Sweden
[16] Jet Propulsion Laboratory, California Institute of Technology, 4800 Oak Grove Dr, Pasadena, CA 91109, USA
[17] MIT Kavli Institute for Astrophysics and Space Research, Massachusetts Institute of Technology, 77 Massachusetts Ave, Cambridge, MA 02139, USA
[18] Department of Physics, Massachusetts Institute of Technology, 77 Massachusetts Ave, Cambridge, MA 02139, USA
[19] Dunlap Institute for Astronomy & Astrophysics, University of Toronto, 50 St. George Street, Toronto, ON M5S 3H4, Canada
[20] Sidrat Research, Toronto, ON, Canada
[21] Instituto de Astrofísica de Canarias, Vía Láctea s/n, E-38200, La Laguna, Tenerife, Spain
[22] GRANTECAN, Cuesta de San José s/n, E-38712, Breña Baja, La Palma, Spain
[23] Department of Physics & Astronomy, University of British Columbia, 6224 Agricultural Road, Vancouver, BC V6T 1Z1, Canada

Abstract

Fast radio burst FRB 20180916B in its host galaxy SDSS J015800.28+654253.0 at 149 Mpc is by far the closest-known FRB with a robust host galaxy association. The source also exhibits a 16.35 day period in its bursting. Here we present optical and infrared imaging as well as integral field spectroscopy observations of FRB 20180916B with the WFC3 camera on the Hubble Space Telescope and the MEGARA spectrograph on the 10.4 m Gran Telescopio Canarias. The 60–90 milliarcsecond (mas) resolution of the Hubble imaging, along with the previous 2.3 mas localization of FRB 20180916B, allows us to probe its environment with a 30–60 pc resolution. We constrain any point-like star formation or H II region at the location of FRB 20180916B to have an Hα luminosity $L_{H\alpha} \lesssim 10^{37} \, \mathrm{erg \, s^{-1}}$, and we correspondingly constrain the local star formation rate to be $\lesssim 10^{-4} \, \mathrm{M_\odot \, yr^{-1}}$. The constraint on Hα suggests that possible stellar companions to FRB 20180916B should be of a cooler, less massive spectral type than O6V. FRB 20180916B is 250 pc away (in projected distance) from the brightest pixel of the nearest young stellar clump, which is ∼380 pc in size (FWHM). With the typical projected velocities of pulsars, magnetars, or neutron stars in binaries (60–750 km s^{-1}), FRB 20180916B would need 800 kyr to 7 Myr to traverse the observed distance from its presumed birth site. This timescale is inconsistent with the active ages of magnetars ($\lesssim 10$ kyr). Rather, the inferred age and observed separation are compatible with the ages of high-mass X-ray binaries and gamma-ray binaries, and their separations from the nearest OB associations.

Unified Astronomy Thesaurus concepts: Magnetars (992); High mass x-ray binary stars (733); Radio transient sources (2008); Hubble Space Telescope (761)

1. Introduction

More than a decade after the discovery of the "Lorimer Burst" (Lorimer et al. 2007), the physical origin(s) of fast radio bursts (FRBs) remains unclear. These bright (∼0.1–100 Jy ms fluence), short-duration (a few μs to 100 ms) radio flashes have been shown to be extragalactic in origin, but it is still unclear what type of object produces them or what the exact emission mechanism might be— see Petroff et al. (2019) and Cordes & Chatterjee (2019) for recent reviews, and Platts et al. (2019) for a catalog of proposed theories. The high brightness temperatures ($T_b \sim 10^{36}$ K) of FRBs point to coherent emission from a compact source with high energy density,

and for this reason many models have invoked neutron stars, white dwarfs, and/or black holes in a variety of possible settings. The fact that some FRB sources are repeating (Spitler et al. 2016), whereas others appear to be one-off events (Shannon et al. 2018), also raises the question of whether the phenomenon can be ascribed to a single source type or whether there are at least two subpopulations with distinct physical natures (Cui et al. 2021).

Detailed spectro-temporal and polarimetric characterization of FRB signals can help constrain models (Farah et al. 2018; Day et al. 2020; Nimmo et al. 2020), as can multiwavelength associations or constraints (Scholz et al. 2017, 2020; Bhandari et al. 2020a). Radio interferometers have now provided robust

host galaxy associations for roughly a dozen FRBs[24]—both repeating and apparently one-off (Chatterjee et al. 2017; Bannister et al. 2019; Prochaska et al. 2019; Ravi et al. 2019; Macquart et al. 2020; Marcote et al. 2020). In principle, the properties of these host galaxies also offer important clues, but thus far a wide range of host galaxy types have been observed (Bhandari et al. 2020b; Heintz et al. 2020; Mannings et al. 2020). FRB models need to accommodate this diversity or resort to multiple populations. High-precision ($\lesssim$100 mas) positions are possible with the Australia Square Kilometre Array Pathfinder (ASKAP; Bannister et al. 2019), Very Large Array (Chatterjee et al. 2017), and European Very-long-baseline-interferometry Network (EVN; Marcote et al. 2017), and allow for localization *within* host galaxies. This can, e.g., confirm or exclude an association with the nucleus of the host galaxy or a region of active star formation.

Insights into the FRB mystery can also come from finding analogous sources in our own Milky Way. The recent discovery of an exceptionally bright ($\sim$1 MJy ms) radio burst (sometimes designated FRB 200428A; CHIME/FRB Collaboration et al. 2020b; Bochenek et al. 2020)—and accompanying hard X-ray burst (Mereghetti et al. 2020; Li et al. 2020; Ridnaia et al. 2020; Tavani et al. 2020)—from the Galactic magnetar SGR 1935+2154 bridges the many orders of magnitude in luminosity between the pulses (regular and giant) of canonical radio pulsars and the extragalactic FRBs. In fact, if placed at the 149 Mpc distance of the closest localized FRB, SGR 1935+2154's bright burst would only be a factor of $\sim$30 times less luminous than the least energetic FRBs seen thus far. This suggests that a significant fraction of FRBs could have a magnetar origin. The discovery of 20–100 Jy ms bursts from SGR 1935+2154 (Kirsten et al. 2020) —bright compared to FRB fluences but far weaker in luminosity —might also suggest that we are only seeing the tip of the burst energy distribution from extragalactic FRBs.

FRB 20121102A (previously FRB 121102; Spitler et al. 2014, 2016) and FRB 20180916B (previously FRB 180916.J0158+65; CHIME/FRB Collaboration et al. 2019b) are currently the two best-characterized repeating FRBs, and the first two to be precisely localized within a host galaxy (Chatterjee et al. 2017; Marcote et al. 2017, 2020; Tendulkar et al. 2017). The spectro-temporal and intrinsic polarimetric properties of bursts from FRB 20121102A and FRB 20180916B are remarkably similar, strongly suggesting that they have the same progenitor type and detailed emission mechanism.

Both sources show the characteristic downward frequency drift between sub-bursts (Hessels et al. 2019), which is seen in bursts from many repeaters (CHIME/FRB Collaboration et al. 2019a, 2019b; Fonseca et al. 2020) and colloquially termed the "sad trombone" effect. FRB 20121102A showed a 30 μs wide burst component at 4.5 GHz (Michilli et al. 2018); a recent study of FRB 20180916B using voltage data finds burst structure down to $\sim$3–4 μs and spanning close to three orders of magnitude up to $\sim$2 ms within individual bursts (Nimmo et al. 2020).

These two repeaters also have indistinguishable polarimetric properties, showing nearly 0% circular polarization, but $\sim$100% linear polarization with a roughly flat polarization angle during and *between* bursts[25] (Michilli et al. 2018; Nimmo et al. 2020).

However, FRB 20121102A shows a drastically higher Faraday rotation measure (RM $\sim 10^5$ rad m; Michilli et al. 2018), which is highly variable (ΔRM $\sim 3 \times 10^4$ rad m^{-2}) on timescales of days to years (Gajjar et al. 2018; Michilli et al. 2018; Hilmarsson et al. 2020). FRB 20121102A also shows clear dispersion measure (DM) variations (ΔDM $\sim$ 3–5 pc cm^{-3}; Hessels et al. 2019; Josephy et al. 2019). In comparison, FRB 20180916B shows a much more stable DM (ΔDM $\lesssim$ 0.1 pc cm^{-3}; CHIME/FRB Collaboration et al. 2020a; Nimmo et al. 2020), and RM variations of only $\sim$2–3 rad m^{-2} (Pleunis et al. 2020).

It has recently also been reported that both sources are periodic in their activity, with FRB 20180916B modulated at $P_{\text{activity}} = 16.33 \pm 0.12$ day (CHIME/FRB Collaboration et al. 2020a; Pleunis et al. 2020) and FRB 20121102A likely modulated at $P_{\text{activity}} \sim 160$ day (Cruces et al. 2021; Rajwade et al. 2020). This could conceivably be related to an orbital period (Ioka & Zhang 2020; Lyutikov et al. 2020; Popov 2020; Zhang & Gao 2020), rotational period (Beniamini et al. 2020), or precession period (Levin et al. 2020; Sob'yanin 2020; Yang & Zou 2020; Zanazzi & Lai 2020).

At first glance, perhaps the most striking difference between these astrophysical sources is their host galaxy and local environment: FRB 20121102A is localized to a low-metallicity dwarf at $z = 0.193$ (Chatterjee et al. 2017; Tendulkar et al. 2017), while FRB 20180916B is found in a massive $10^{10} M_\odot$ spiral at $z = 0.0337$ (Marcote et al. 2020). Both sources are found in close proximity to a prominent star-forming region (Bassa et al. 2017; Marcote et al. 2020), though FRB 20121102A's $\sim$10 milliarcsecond (mas) localization (Marcote et al. 2017), Hubble Space Telescope (HST) imaging (Bassa et al. 2017), and adaptive optics observations (Kokubo et al. 2017) demonstrate that it is offset by $\sim$200 pc from the peak of star formation in this region.[26] Lastly, the association of FRB 20121102A with a persistent (isotropic luminosity $\sim 10^{39}$ erg s^{-1}) and compact ($<$0.7 pc) radio source (Chatterjee et al. 2017; Marcote et al. 2017) stands in stark contrast to the lack of such a counterpart to FRB 20180916B (Marcote et al. 2020), despite it being significantly nearer to Earth.

At a luminosity distance of 149 Mpc, FRB 20180916B is by far the closest-known FRB with a robust host galaxy association (Marcote et al. 2020). It is also the most precisely localized FRB to date: EVN observations achieved a 2.3 mas localization within the International Celestial Reference Frame (ICRF), including systematic uncertainties (Marcote et al. 2020). FRB 20180916B thus provides an unprecedented opportunity for high-resolution optical studies of its local environment. In previous Gemini North observations, FRB 20180916B was associated with the apex of an apparently "V"-shaped star-forming region (or complex of closely spaced star-forming regions) with an extent of $\sim$2″. Given the 0″.8–1″.0 seeing of those observations, higher-resolution observations can greatly enhance our understanding of FRB 20180916B's local environment, and perhaps even detect a massive binary companion that could elucidate its periodic activity.

Here we present an imaging and spectroscopic study of the immediate environment of FRB 20180916B using observations from HST and the 10.4 m Gran Telescopio Canarias (GTC). These observations probe 60 pc scales within the host galaxy— by far the closest view of any FRB source to date. We present

---

[24] http://frbhosts.org/

[25] However, another repeating source, FRB 20180301A (previously FRB 180301), was recently shown to have diverse polarization swings and polarization fractions in different bursts (Luo et al. 2020), showing that FRB 20180916B and FRB 20121102A are not necessarily representative of the whole repeater population.

---

[26] Yet another repeater, FRB 20190711 (Macquart et al. 2020), is also found in a massive $8 \times 10^9 M_\odot$ star-forming galaxy (Heintz et al. 2020) though the localization of the FRB is too imprecise to identify its local environment.

Table 1
Observation Details

Obs. Date (UTC)	Instrument/ Camera	Grating/ Filter	Exp. Time (s)	Obs. ID[a]	Notes[b]
Gran Telescopio Canarias (Program GTC18-19BMEX)					
2019-09-24	MEGARA/IFU	LR-R	680	2303712	AM = 1.27, seeing = $1''.0$
2019-09-24	MEGARA/IFU	LR-R	680	2303713	AM = 1.26, seeing = $1''.0$
2019-09-24	MEGARA/IFU	LR-R	680	2303714	AM = 1.26, seeing = $1''.0$
Hubble Space Telescope Program (16072)					
2020-07-16	WFC3/UVIS1	F673N	2877	IE8Q01010	resolution = $0''.058$
2020-07-17	WFC3/UVIS1	F657N	2877	IE8Q02010	resolution = $0''.056$
2020-07-17	WFC3/IR	F110W	306	IE8Q03010	resolution = $0''.095$
2020-07-17	WFC3/IR	F110W	5623	IE8Q03020	resolution = $0''.095$

Notes.
[a] Observation ID for the GTC Archive https://gtc.sdc.cab.inta-csic.es/gtc/jsp/searchform.jsp and the HST MAST Archive https://archive.stsci.edu/index.html.
[b] Airmass (AM) and seeing conditions, and FWHM of the point-spread function for WFC3. The size of the spaxel for MEGARA observations is $0''.62$.

the observations and analysis in Sections 2 and 3, respectively, and discuss the astrophysical implications and interpretation in Section 4.

2. Observations and Reduction

We observed FRB 20180916B using the Multi-Espectrógrafo en GTC de Alta Resolución para Astronomía (MEGARA) integral field spectrograph on the GTC and the Wide Field Camera 3 (WFC3) instrument on HST in 2019 September and 2020 July (Table 1). Here we describe the observations and data reduction procedures.

2.1. MEGARA

Observations of SDSS J015800.28+654253.0 were performed with the MEGARA instrument (Carrasco et al. 2018; Gil de Paz et al. 2018) at the 10.4 m GTC in 2019 September (see Table 1 for details). We used the large compact bundle integral field unit mode (LCB IFU), which provides a field of view (FoV) of $12''.5 \times 11''.3$ and a spectral pixel (spaxel) size of $0''.62$ ($\equiv 450$ pc at 149 Mpc). The observations were carried out using the LR-R setup with a spectral coverage of 6100–7300 Å. The pointing was set so that the MEGARA FoV covered both the "V"-shaped structure found near FRB 20180916BB and the nucleus of the host galaxy (see Figure 1(a)). During the run we also observed the spectro-photometric standard star HR 7596, and acquired halogen lamp flats and ThNe arcs using the MEGARA Instrument Calibration Module (ICM), as well as a series of bias images.

The data were processed using the development version (v0.9.2) of the MEGARA Data Reduction Pipeline[27] (DRP; Pascual et al. 2018, 2019), which is based on a series of processing recipes, and the cookbook.[28] The halogen lamp observations allowed us to trace the spectra (`TraceMap` recipe), to recover the flux of each fiber affected by cross-talk contamination from adjacent fibers (`ModelMap` recipe), and to correct for changes in sensitivity from blue to red in between fibers (`FiberFlat` recipe). Prior to the correction by fiber-flat, we wavelength-calibrated the images (including the master fiber-flat), fiber by fiber, using ThNe arc observations obtained with the

MEGARA ICM. The `LcbStdStar` recipe allowed us to use the LCB observations of the standard stars to derive the system response function after assuming the La Palma extinction curve.[29] The results from all these recipes were finally used (`LcbImage` recipe) to process the SDSS J015800.28 +654253.0 data. The sky background subtraction was performed using the processed fiber spectra of the eight fixed seven-fiber minibundles (56 fibers) that are mounted on the LCB pseudo-slit and that are placed in a blank sky region $1'.75$–$2'$ away from the center of the LCB (which is also the optical axis of the instrument). The final product of this data reduction is a row-stacked spectra (RSS hereafter) FITS file that is wavelength- and flux-calibrated and has its sky background subtracted.

2.2. WFC3

The host galaxy of FRB 20180916B was observed with the WFC3 instrument on the HST in the F657N (6476–6674 Å) and F673N (6681–6880 Å) filters of the UVIS channel, as well as the F110W filter (8832–14121 Å, IR channel) on 2020 July 16 and 17. Table 1 summarizes the observations. The aim of the F110W observations was to detect or constrain the presence of bright stars or stellar clusters and to understand the morphology of the environment. At the redshift $z = 0.0338$ of the host galaxy, the Hα line is shifted to 6784 Å (within the F673N filter coverage) while the zero-redshift Hα filter, F657N, is used as an Hα-off filter to constrain the underlying continuum. The Hα-on and -off images are acquired to constrain local star formation and understand the distribution of atomic hydrogen in the region. At 149 Mpc, the angular and spatial resolution of the F657N, F673N, and F110W filters is 56 mas $\equiv$ 40 pc, 58 mas $\equiv$ 42 pc, and 95 mas $\equiv$ 68 pc, respectively.

The UVIS observations were undertaken with three exposures of 959 s each (total 2877 s), dithered in the three-point dither pattern (`WFC3-UVIS-DITHERLINE-3PT`) to optimally sample the point-spread function. A post-exposure flash adjusted for nine electrons was used to minimze losses from charge transfer efficiency (CTE), as recommended by the WFC3/UVIS data handbook[30] The IR observations were undertaken with 10 exposures with a four-point dither pattern

---

[27] https://github.com/guaix-ucm/megaradrp
[28] http://www.gtc.iac.es/instruments/megara/media/MEGARA_cookbook_1I.pdf
[29] https://www.ing.iac.es/Astronomy/observing/manuals/ps/tech_notes/tn031.pdf
[30] https://hst-docs.stsci.edu/wfc3dhb
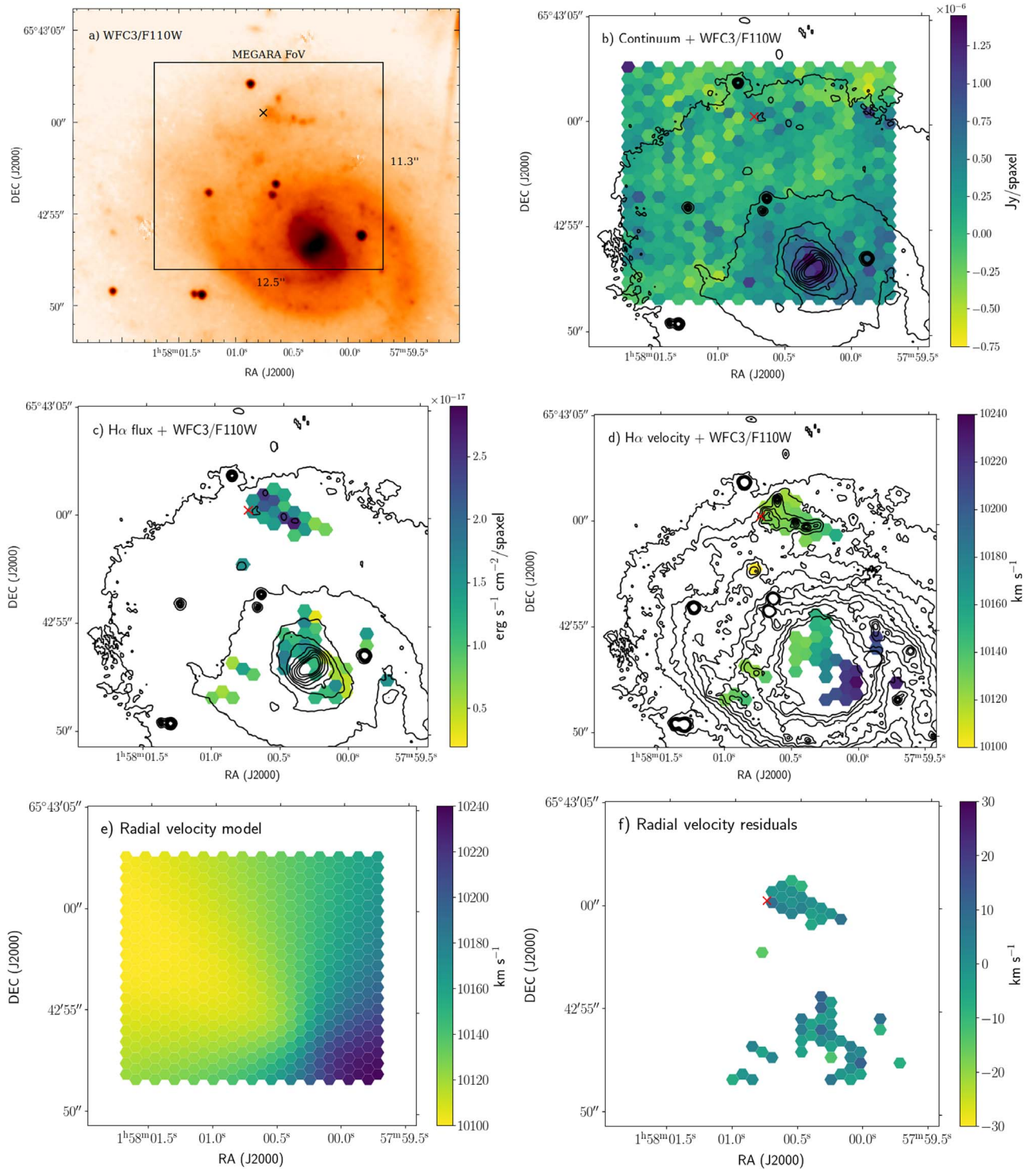
Figure 1. (a) A section of the HST F110W image illustrating the MEGARA FoV. The position of FRB 20180916B is shown by a cross (as well as on the three subsequent panels). (b) Average continuum flux level (in Jy/spaxel) from the LR-R setup observations within the spectral range between 6100 and 7200 Å. The contours of the F110W image ranging from 0.02 to 0.47 e$^-$ s^{-1} pixel^{-1} (or between 1.36×10^{-9} and 3.2×10^{-8} Jy pixel^{-1}) in intervals of 0.05 e$^-$ s^{-1} pixel^{-1} are overlaid. (c) Hα flux of those spaxels with S/N $\geqslant$ 5 at the peak of the line relative to the continuum rms with the F110W contours overlaid. The contours shown here are identical to those drawn in panel (b). Note that the three brightest (in Hα) spaxels in the "V"-shaped region coincide with local maxima in the F110W band. These regions have been used to properly correct the astrometry of the MEGARA LCB data (see text for details). (d) Hα radial velocity data with F110W contours overlaid, ranging from 0.02 to 0.11 in intervals of 0.01 e$^-$ s^{-1}. (e) Best-fitting purely rotating, inclined thin-disk kinematic model (see text). (f) Residuals of the radial velocity after the best-fitting thin-disk model has been subtracted from the observed Hα radial velocities. The best-fitting rms velocity is only 5.7 km s^{-1}.

(`WFC3-IR-DITHERBOX-MIN`) read out with the `SPARS50` readout sequence, for a total exposure of 5929 s.

The precalibrated and CTE-corrected UVIS and IR (`.FLC` and `.FLT`, respectively) images were distortion-corrected and astrometrically aligned to the ICRF using the Gaia DR2 catalog (Gaia Collaboration et al. 2016, 2018) and the `tweakreg` tool. The images were individually aligned using 60–90 stars (UVIS images) and 30–35 stars (IR images) to achieve typical astrometric

rms residuals of 18 mas and 36 mas in the UVIS and IR images, respectively. The alignment error between the Gaia optical reference frame and the ICRF defined with radio sources is negligible in this context.

The aligned images were combined using `astrodrizzle` to make cosmic-ray-rejected images with a final platescale of 30 mas pixel^{-1}. Photometry was performed on the aligned, individual exposures (`dolphot` Dolphin 2016) using the appropriate point-spread functions for each filter.

There is no point source detected at the location of FRB 20180916B. To constrain the detectable source brightness, including the underlying diffuse emission from the host galaxy, we used the `addstars` tool to add simulated point sources at the location of FRB 20180916B with a range of brightnesses and calculated the detection significance through `dolphot` in each filter.

We use the absolute photometric calibration as defined by the WFC3 calibration team,[31] which has systematic errors of $\approx 2\%$ (F110W) and $\sim 10\%$ (F657N, F673N).

3. Analysis and Results

3.1. IFU Spectroscopy

In Figure 1(b) we present the distribution of the continuum emission obtained by averaging the flux of the RSS in the wavelength range between 6100 and 7200 Å. We note that the fluxes shown here are per spaxel in the case of MEGARA and per pixel in the case of the HST WFC3/F110W image. In order to derive the emission-line properties of the area of the SDSS J015800.28+654253.0 galaxy covered by our MEGARA LCB observations, we made use of custom Python 3 code based on the `lmfit` package. This code allows one to simultaneously fit a linear local continuum and the emission-line profile (as a Gauss–Hermite series) for each LCB spaxel. The code generates an output RSS where each channel corresponds to a different property (line flux, equivalent width, radial velocity, etc.). In panel (c) we show the results of the analysis of the Hα line adopting a single Gaussian profile for all spaxels with a signal-to-noise ratio (S/N) at the peak of the line relative to the rms of the continuum of S/N ⩾ 5. This figure shows, on one hand, the presence of line emission associated with the nuclear spiral and, on the other hand, a series of bright, high-surface-brightness emission-line clumps associated with the brightest regions of the "V"-shaped structure located ∼7″ north of the center of the galaxy. The compactness of these three regions both in HST images and in the MEGARA line-emission data was used to perform a correction of 0″.9 east and 1″.5 south to the MEGARA astrometry. In panel (d) we provide the radial velocities of the ionized gas as given by Hα for the same S/N ⩾ 5 spaxels. Here we can clearly see that most of the east side of the galaxy shows approaching velocities compared to the nucleus of the galaxy, suggesting that the kinematic minor axis is approximately located in the north–south direction. It is also important to emphasize that the "V"-shaped structure shows a radial velocity in Hα that does not differ much from that of the rest of the galaxy, especially if we take into account the fact that the purely rotating gas in that part of the galaxy is moving toward us (see Section 3.1.1 for more details). The best-fitting systemic barycentric velocity is $10{,}190^{+8}_{-4}$ km s^{-1}, leading to the redshift

$z = 0.03399$. This result is consistent with that presented by Marcote et al. (2020).

Apart from Hα we detect [N II] $\lambda 6584$, [S II] $\lambda 6717$, and [S II] $\lambda 6731$ lines in the combined spectrum of all spaxels with S/N > 5 at the peak of the Hα line. The [N II] $\lambda 6584$/Hα ratio (N2 = log[N II]/Hα = −0.745) can be used to estimate the ionized gas metallicity in this region of the galaxy $12 + \log[O/H] = 8.4 \equiv Z_{\odot}/2$ (Marino et al. 2013). In the 19 spaxels to the immediate west of FRB 20180916B the N2 ratio is measured to be N2 $= -0.73^{+0.1}_{-0.2}$, consistent with the galaxy-wide average measured above.

The radial velocity measurement above and the kinematic modeling below focus on Hα since it is brightest and most precisely measured. Measuring the radial velocity differences between the [N II] and Hα lines in individual spaxels, we find that the mean and rms velocity difference is 1.5 ± 8.4 km s^{-1}. The rms is dominated by the uncertainties in radial velocity from each [N II] line measurement.

3.1.1. Kinematic Modeling of the Host Galaxy

In order to test the hypothesis that the gas in the "V"-shaped structure located near the FRB position is actually participating in the overall rotation of the gas in the disk, we have built a thin-disk kinematic model assuming a fixed inclination (i) at all galacto-centric distances R and a rotation curve parameterized as $a \times \arctan(b \times R)$. The inclined rotating disk model is then projected onto the sky plane, where a radial velocity is calculated for every spaxel's location. We then explored a wide range of parameters (i, position angle, R.A.$_{\rm center}$, decl.$_{\rm center}$, $V_{\rm sys}$, a, b) and derived the model that yields the minimum sum of the quadratic differences between data and model. The inclination, which is poorly constrained given the sparse information on radial velocities for this object, was adopted to be the photometric one $(33° \pm 6°)$ as measured from imaging data in the next section after assuming an axisymmetric disk. The rms of the residual obtained is 5.7 km s^{-1} for a kinematical position angle of $239.9° \pm 1.5°$ and a best-fitting rotation curve $a = 94 \pm 5$ km s^{-1} and an inverse "core" radius of $b = 1.04^{+0.11}_{-0.13}$ arcsec^{-1} (all errors are 1σ). Figure 2 shows the covariance in the disk parameters. The best-fitting model and the corresponding residuals are shown in panels (e) and (f) of Figure 1, respectively. The homogeneity and low amplitude of the residuals shown in panel (e) indicate that all regions detected in Hα can be reproduced by a simple thin-disk, purely rotating kinematic model.

3.2. High-resolution Imaging

Figure 3 shows the $1' \times 1'$ field around FRB 20180916B in the HST F110W filter (top left) and the $5'' \times 5''$ zoomed-in fields (marked by the dashed black box) in the F110W (top right), F673N (bottom left, Hα-on), and F657N (bottom right, Hα-off) filters. The images are centered at the location of FRB 20180916B with a green ellipse (pointed to by the green arrow) showing the astrometric uncertainties in the localization and radio-to-optical frame registration of 36 mas.

FRB 20180916B is located off the vertex of the "V"-shaped structure that lies along the spiral arm of SDSS J015800.28 +654253.0. The "V"-shaped structure is indicated in the top left panel of Figure 3. The vertex of the "V" has an emission region with FWHM size of approximately 0″.27, corresponding to about 190 pc. The region's shape and the underlying background emission has complex structure, making it challenging to describe

---

[31] https://www.stsci.edu/hst/instrumentation/wfc3/data-analysis/photometric-calibration
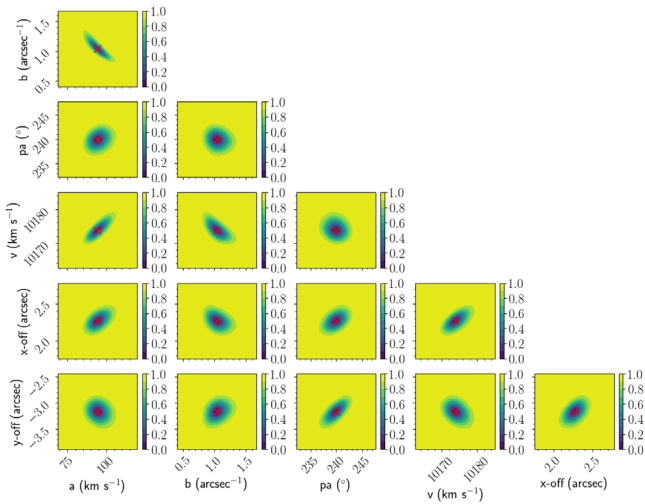
Figure 2. Confidence regions of the disk modeling parameters are shown. The red cross shows the best-fit model. The 1σ confidence intervals in the text correspond to the 68% contours in each panel of this corner plot.

with a single number. This size has not been corrected for the $0\rlap{.}{''}095$ resolution of the F110W image—we expect the region to be more compact. The region is not bright in Hα and is barely detectable in the F673N image. The Hα luminosity and the star formation surface density of the vertex are discussed in Section 3.3. We assume that the F110W light also traces the Hα distribution within the vertex region, hence the brightest F110W pixel likely has the highest star formation density.

FRB 20180916B is $0\rlap{.}{''}355$, i.e., $\sim$250 pc, away from the brightest pixel in the F110W image. The offset is similar to the $\sim$200 pc separation of FRB 20121102A from the center of the Hα knot in its host galaxy (Bassa et al. 2017; Kokubo et al. 2017). The 380 pc size of the star-forming region for FRB 20180916B is much smaller than the 1.4–1.9 kpc size of the star-forming knot hosting FRB 20121102A (Bassa et al. 2017; Kokubo et al. 2017). The magnitude of this offset compared to the offsets of other compact objects (either isolated or in binaries) from their birth sites sets strong constraints on the age and nature of FRB 20180916B, as discussed in Section 4.

FRB 20180916B is located in the plane of the Milky Way toward the anticenter. The Bayestar19 (Green et al. 2019) estimate for the reddening between the g' and r' filters is $E_{g-r} = 0.69 \pm 0.02$ (1σ) based on the PanSTARRs, Two Micron All Sky Survey, and Gaia data. We follow the scaling prescribed by Green et al. (2019), and the recalibrated extinction law in Schlafly & Finkbeiner (2011), to estimate the extinction in the F110W and the F673N filters to be 0.61 mag and 1.37 mag, respectively.[32]

The host galaxy extinction is assumed to be negligible, considering its nearly face-on orientation, for the IR wideband imaging (F110W). However, the conversion of Hα flux to star formation rate includes a correction for the typical host extinction (Kewley et al. 2002).

We also performed a surface photometry analysis on the F110W HST image using the `photutils.isophote` package of `Astropy`. The package estimates the isophotes using the

method described in Jedrzejewski (1987). By assuming an intrinsically axisymmetric, infinitesimally thin disk, we estimate the inclination angle of the stellar disk, $i_{\rm stellar} = 33^\circ \pm 6^\circ$ (1σ), which is in agreement with the inclination angle estimated using the Hα data. In estimating $i_{\rm stellar}$, we only considered the range of projected galactocentric radius between 4 and 10 kpc because at radii <4 kpc the radial profile traces the bulge of the galaxy, and beyond 10 kpc the fitted ellipticity values show large swings.

3.3. Star Formation

The 5σ limit for Hα emission from a point source at the location of FRB 20180916B (above the diffuse emission of the host galaxy) is 25.42 mag (Vega). Assuming the continuum to be negligible and all the light to be due to the redshifted Hα photons, this corresponds to a flux limit of $3 \times 10^{-18}\,{\rm erg\,cm^{-2}\,s^{-1}}$ after correcting for the Milky Way extinction. This corresponds to a point-source Hα luminosity of $8 \times 10^{36}\,{\rm erg\,s^{-1}}$. Using the conversions of Kewley et al. (2002), the star formation rate at the location of FRB 20180916B is constrained to be $\lesssim 10^{-4}\,M_\odot\,{\rm yr^{-1}}$. The resolution ($\lambda/D$) of the F673N image is $\approx$58 mas. Given this size scale, the star formation surface density at the location of FRB 20180916B should be $\lesssim 2 \times 10^{-2}\,M_\odot\,{\rm yr^{-1}\,kpc^{-2}}$.
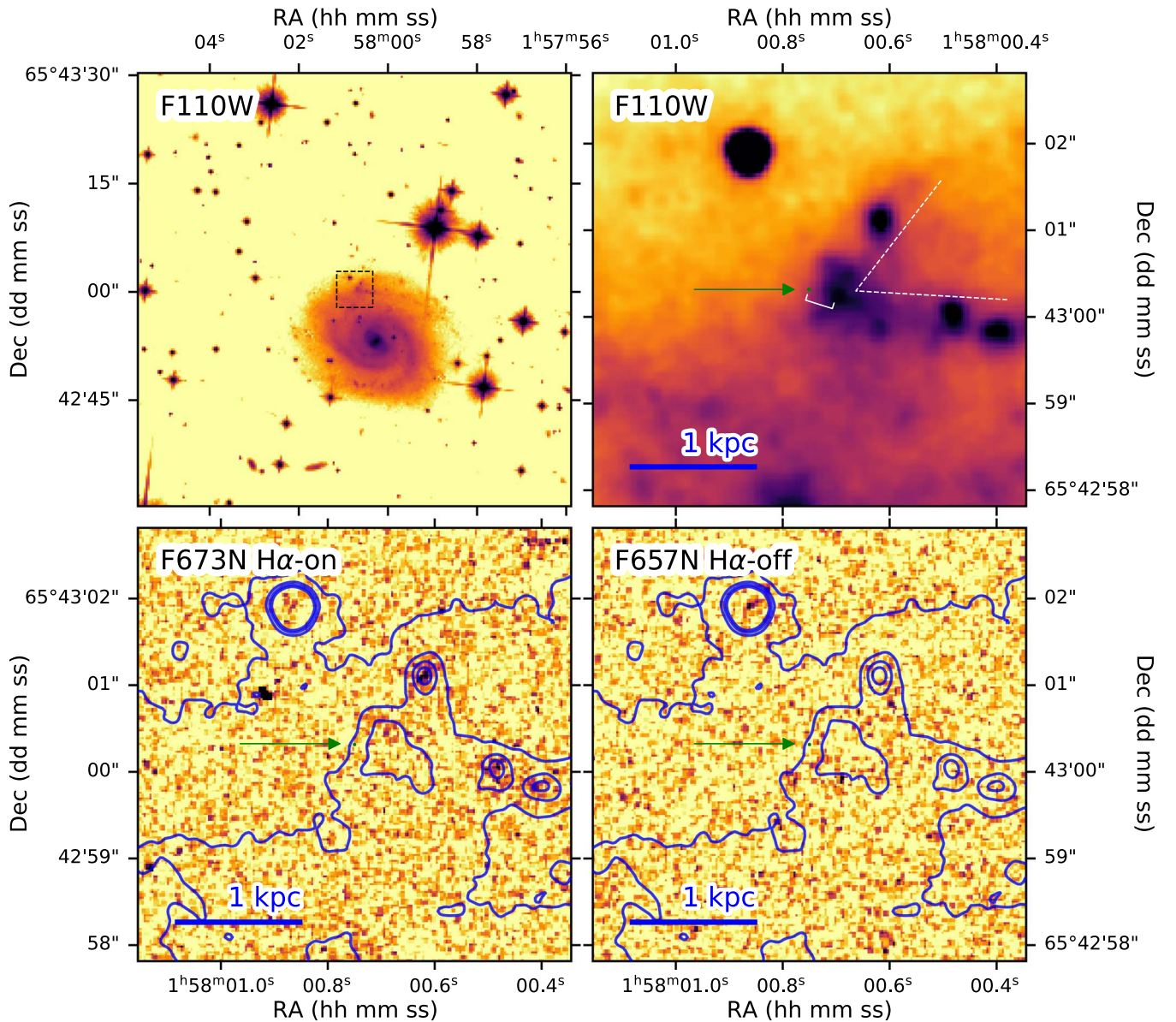
The nebular region at the vertex of the "V" is measurably extended in the F110W and F673N images. To measure the total star formation rate in the region, we smoothed the F673N image with a Gaussian kernel with $\sigma = 125$ mas, revealing a detectable blob with a total extinction-corrected flux of $\approx 3 \times 10^{-17}\,{\rm erg\,cm^{-2}\,s^{-1}}$, corresponding to an H$\alpha$ luminosity $\approx 9 \times 10^{37}\,{\rm erg\,s^{-1}}$ and a star formation surface density of $3 \times 10^{-2}\,M_\odot\,{\rm yr^{-1}\,kpc^{-2}}$. The measurement assumes a photometric zero-point at infinite radius. This is roughly consistent with the extinction-corrected Hα flux of $5.5 \times 10^{-17}\,{\rm erg\,s^{-1}}$ measured in the 620 mas wide MEGARA spaxel located at the vertex of the "V". The difference in the flux measurement is likely due to extra emission outside the HST photometric region in the wings of the Hα clump.

3.4. H II Regions and O/B stars

In the HST F110W image, we constrain a point source at the location of FRB 20180916B to be fainter than 27.15 mag (Vega). Including the extinction correction discussed above and the distance modulus of SDSS J015800.28+654253.0, this corresponds to an absolute magnitude limit of $M_{\rm F110W} > -7.97$ mag (Vega). The J-band magnitude of an O3V star is ≈ -4.9 mag (Worthey & Lee 2011; Pecaut & Mamajek 2013). Thus, the F110W data are unable to constrain the presence of single bright stars.

However, the upper limit on the Hα luminosity at the location of FRB 20180916B can constrain the rate of ionizing photons in the neighborhood. Gutiérrez et al. (2011) demonstrated a tight correlation between the Hα luminosity L_α and radius for H II regions in M51 and NGC 4449. An H II region with $L_\alpha < 10^{37}\,{\rm erg\,s^{-1}}$ is expected to be smaller than 10–60 pc (including the scatter in the relation). Consequently, we do not expect that our non-detection of an H II region in the F673N image is because the Hα flux is resolved out.

The L_α limit can be converted to a limit on the hydrogen ionizing flux $Q(\rm H^0) < 9 \times 10^{48}\,{\rm s^{-1}}$ (see Osterbrock & Ferland 2006, for conversion constants). From the $Q(\rm H^0)$ calculations of Martins et al. (2005), we can rule out a single main-sequence

---

[32] We note that the older extinction map from Schlafly & Finkbeiner (2011), based on Sloan Digital Sky Survey photometry, estimates the F110W extinction to be 0.87 mag along this line of sight. The discrepancy between the older and newer estimates does not qualitatively affect our conclusions, and hence we use the newer estimates from Green et al. (2019).

Figure 3. HST observations of FRB 20180916B's host galaxy. The $60'' \times 60''$ F110W image (top, left) shows the full image of SDSS J015800.28+654253.0 and its surroundings. The dashed black box denotes the $5'' \times 5''$ region shown in the zoomed-in images: F110W (top right), F673N (bottom left, Hα-on), and F657N (bottom right, Hα-off). The position of the FRB source, including the astrometric uncertainties in its localization and radio-to-optical frame transfer, is shown by the green ellipse at the center of each zoomed-in figure (pointed to by the green arrow). The blue bar indicates the angular scale corresponding to 1 kpc at the distance of SDSS J015800.28+654253.0. The F110W zoomed-in image is annotated to show the "V"-shaped structure and the $0\rlap{.}''355$ separation between FRB 20180916B and the center of the nearest Hα blob. The F673N and F657N images are overplotted with F110W intensity contours to guide the eye. The color scale of each image is inverted.

star hotter than O6V. For giants and supergiants, stars hotter than O7.5III and all OI stars are ruled out.

4. Discussion

Our observations and constraints on the environment of FRB 20180916B set it apart from the other localized FRBs, and challenge some of the theoretical models put forward to explain its periodic activity. Here we discuss the observational and theoretical implications of these constraints.

4.1. Comparison to FRB 20190608B

FRB 20190608B (previously FRB 190608; Macquart et al. 2020) is an apparently non-repeating FRB that was detected and localized by ASKAP to a spiral host galaxy, SDSS J221604.90 −075356.0, at a redshift of $z = 0.11778$. The location of FRB 20190608B in the spiral arm of SDSS J221604.90 −075356.0, a face-on spiral, is strikingly similar to that of FRB 20180916B. Chittidi et al. (2020) acquired integral field spectra and HST imaging of the host galaxy and measured a local star formation surface density of $1.2 \times 10^{-2}\, M_\odot\, \mathrm{yr}^{-1}\, \mathrm{kpc}^{-2}$ at the location of FRB 20190608B. This is similar to the star formation density in the Hα blob at the vertex of the "V"-shaped structure but significantly higher than the star formation density at the location of FRB 20180916B. The localization precision of FRB 20190608B of $\approx 0\rlap{.}''26$ (1σ) corresponds to a physical scale of 0.55 kpc at the redshift of $z = 0.11778$. Hence, any offset from the star-forming region, similar to that seen for

FRB 20180916B and FRB 20121102A, cannot be measured unless repeat bursts are detected and localized with milliarcsecond precision. Similar to FRB 20190608B, FRB 20180916B is also not found to be coincident with or near the brightest star-forming region in the host galaxy. While Chittidi et al. (2020) noted the spectral and the mass differences between the host galaxies, the local environments of FRB 20180916B, a repeater, and FRB 20190608B, an as-yet non-repeater,[33] are very similar. Continued monitoring for repeat bursts from FRB 20190608B would help to improve its localization and to refine the comparison of its nature with that of FRB 20180916B.

4.2. Nature of FRB 20180916B

The high-resolution, multiband optical imaging and spectroscopy we present here provide important insights into the nature of FRB 20180916B, which complement what can be discerned from the spectro-temporal and polarimetric properties of the bursts themselves—as well as the periodic activity of the source. We first summarize what was known previously, and then discuss the implications of the new results we present here.

4.2.1. Previous Results

Observations of $\sim$3–4 μs burst structure place tight constraints on the size of the emitting region (Nimmo et al. 2020); in the absence of special relativistic effects, this corresponds to a $\sim$1 km region, given light-crossing-time arguments. In the context of magnetar models, this short timescale, along with the range of observed temporal timescales spanning 3–4 orders of magnitude from microseconds to milliseconds (Nimmo et al. 2020), is more naturally explained in terms of emission generated relatively close to the neutron star (Beniamini & Kumar 2020; Lyutikov et al. 2020; Lu et al. 2020)—as opposed to much further out in a relativistic shock (Beloborodov 2017; Margalit & Metzger 2018).

The 16.35 day activity period is also a key insight, and differentiates FRB 20180916B from the isolated Galactic magnetar, and putative FRB source, SGR 1935+2154. If FRB 20180916B is produced by a strongly magnetized neutron star, some extra ingredient is necessary to understand the emission mechanism. The activity period could in principle be related to rotation (Beniamini et al. 2020), precession (Levin et al. 2020; Sob'yanin 2020; Yang & Zou 2020; Zanazzi & Lai 2020), or an orbit (Ioka & Zhang 2020; Lyutikov et al. 2020; Mottez et al. 2020). The near-constancy of polarization angle within and *between* bursts places strong constraints on precession models (Nimmo et al. 2020). The similar constraints imposed by the constant polarization angle of FRB 20121102A (Michilli et al. 2018) argue that precession models are disfavored. The variation in rotation measure, which may correlate with orbital phase (Pleunis et al. 2020), suggests the presence of a variable magneto-ionic medium around the system, which is naturally explained in an orbiting binary model. See Pleunis et al. (2020) also for a longer discussion of how the observed frequency dependence of observed burst activity could be interpreted in the context of a binary model.

4.2.2. Constraints from This Work

First, the radial velocity measurements and kinematic modeling from the MEGARA observations show that the "V"-shaped structure is dynamically a part of the spiral galaxy and excludes the possibility that the ionized gas that we detect belongs to a satellite galaxy—a possibility discussed in Marcote et al. (2020), when only seeing-limited images and single-slit spectroscopy of the galaxy were available.
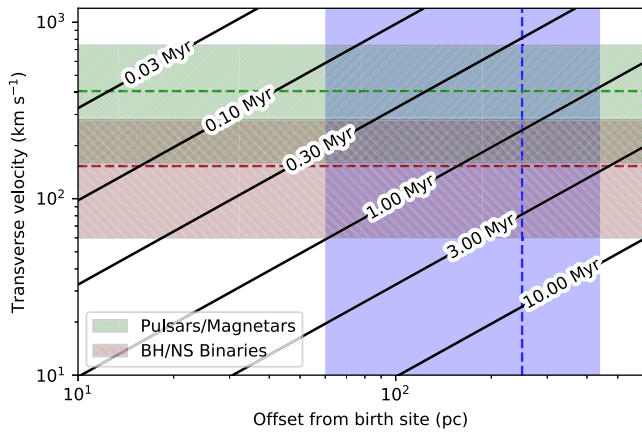
Our Hα on/off observations constrain the Hα luminosity of an unresolved H II region at the location of FRB 20180916B to be $<8 \times 10^{36}\,\mathrm{erg\,s^{-1}}$. The H$\alpha$ luminosities of H II regions range from 10^{34} to $10^{38}\,\mathrm{erg\,s^{-1}}$ (Fich et al. 1990; Azimlu et al. 2011), with the "knee" of the distribution being $10^{36.7}\,\mathrm{erg\,s^{-1}}$. Thus we can rule out the brightest H II regions powered by the youngest massive stars. Specifically, based on the rate of ionizing photons and the corresponding Hα luminosity, we can constrain a possible stellar companion to FRB 20180916B to be cooler and smaller than O6V and O7.5III spectral types. All supergiant O stars can be ruled out. Hα emission-line stars (late O or B spectral types), which have typical Hα luminosities of 10^{32}–$10^{34}\,\mathrm{erg\,s^{-1}}$ (Apparao & Tarafdar 1997), cannot be ruled out by these observations.

Our HST observations demonstrate that FRB 20180916B is offset by 250 ± 190 pc from the nearest knot of active star formation in the host galaxy. The separation is measured from the brightest pixel of the F110W image. Bassa et al. (2017) found a comparably large, $\sim$200 pc offset for FRB 20121102A. This is problematic for models that require a young magnetar (age of $\sim$10–10^5 yr), since such sources are invariably found close to their birth sites. For comparison, the scale height of Galactic magnetars is only 20–30 pc (Olausen & Kaspi 2014). While scale heights are measured perpendicular to the plane of the Galaxy and the offset measured for FRB 20180916B is in the plane of its host, the comparison is valid since natal kicks for magnetars are statistically isotropic. Figure 4 shows the expected age of FRB 20180916B given the range of possible offsets and the typical velocities of pulsars, magnetars, and X-ray binaries in the Milky Way. With the typical projected velocities of pulsars, magnetars, or neutron stars in binaries (60–750 km s^{-1}), FRB 20180916B would need 800 kyr to 7 Myr to traverse the observed distance from its presumed birth site. Even with a kick velocity of $\sim$1000 km s^{-1} at birth, a neutron star would still require $\sim$0.25 Myr to traverse the 250 pc offset we determine for FRB 20180916B.

It is possible that a putative young magnetar was born at the edge of the star-forming region and did not have to travel very far from its birth site. However, such a magnetar is more likely to originate in a region with a higher density of massive star progenitors (i.e., the center of the cluster) rather than at the edges. It is not straightforward to quantify this probability distribution based on the F110W and F673N images. Hence, we show only the distance from the brightest pixel and an approximate size for the cluster in Figure 4, but the probability distribution is not uniform across the range.

Though magnetars may also be created in compact-binary mergers or accretion-induced collapse—as opposed to the core collapse of a massive star—such channels have a much lower rate, and thus our findings suggest that FRB 20180916B is associated with a much older (millions of years) neutron star. Nonetheless, the relative proximity of star formation—in fact a very striking complex of star-forming regions in the host

---

[33] Day et al. (2020) have shown that FRB 20190608B showed some properties similar to repeater bursts—it had a high degree of linear polarization, a non-varying position angle through the burst, and possible complex structure underneath the scattering tail.

Figure 4. Constraints on the age of FRB 20180916B based on the proper motions of isolated neutron stars and those in binaries. The transverse offset from the peak of the nearest Hα blob (vertical dashed blue line) and the range of offsets from the presumed birth site (blue region) are shown. The range is determined by the FWHM of the blob size in the F110W image along the line joining the FRB location to the brightest pixel. The 90% ranges of 1D velocities of pulsars (Hobbs et al. 2005) and magnetars (Tendulkar 2014; Ding et al. 2020) and of neutron stars in binaries (Bodaghee et al. 2012), assuming a Maxwellian distribution, are also shown (green and maroon regions, respectively). The median velocities are shown by dashed lines. Diagonal black lines indicate the ages corresponding to a given offset and velocity.

galaxy—is unlikely to be pure coincidence and suggests that FRB 20180916B is not a very old ($\gtrsim$10–50 Myr) system.

Another possibility is that a neutron star/magnetar is created in situ from the supernova of a runaway OB star (see Zinnecker & Yorke 2007, for a review)—a massive star ejected from a dense stellar cluster through binary interactions at high velocities ($>$30 km s^{-1}). The neutron star/magnetar would be observed to be well separated from the stellar cluster but be young enough to create its own energetic phenomena. However, the challenges with this channel are twofold. First, runaway OB stars represent a small fraction of the population of OB stars (1%–10%; Fujii & Portegies Zwart 2011), and magnetars are a small fraction of the population of neutron stars (10% of core-collapse rate; see Kaspi & Beloborodov 2017), so this channel has low likelihood. Second, given the speeds of these runaway stars (30–120 km s^{-1}), they would still require many millions of years to achieve the observed physical offset, which is a significant fraction of, if not greater than, the lifetimes of O stars. However, B stars, which have longer lifetimes, are still possible.

The Galactic population of high-mass X-ray binaries (HMXBs; Walter et al. 2015) and γ-ray binaries (Dubus 2013) presents a potentially interesting analogy. These systems feature a neutron star and high-mass O- or Be-star companion and have orbital periods that are comparable to FRB 20180916B's 16.35 day activity period—e.g., 1FGL J1018.6−5856 (P_{orb} = 16.6 day) and LSI +61°303 (P_{orb} = 26.5 day). Bodaghee et al. (2012) consider the spatial correlation of HMXBs and active OB star-forming complexes in the Milky Way. They find that the locations of HMXBs reflect the distributions of the massive star-forming regions that are expected to produce them. However, they also determine an average offset of 0.4 ± 0.2 kpc between HMXBs and OB associations, which they attribute to natal kick velocities of 100 ± 50 km s^{-1} and typical system ages of ~4 Myr.

Safarzadeh et al. (2020) analyzed the star formation rate and the separations of FRBs from the centers of their host galaxies (host offsets) for 10 FRBs with secure host associations and

compared them to a simple model where FRB rates are proportional to the recent star formation rate (as expected for prompt magnetars). They reported that the star formation rates measured from the host galaxies are incompatible with such a model but the host offset distribution is compatible. Bochenek et al. (2021) did a similar study comparing the properties and offsets of FRB hosts to those of core-collapse supernovae, and showed that the star formation rates and stellar masses of localized FRB hosts as well as host offsets can be consistent with an origin in magnetars formed from core-collapse supernovae. However, we note that the population of young neutron star binaries would follow the star formation rate and stellar mass distributions to a similar degree to magnetars born in core-collapse supernovae. This highlights the need for precise localization of FRBs: it is not sufficient to know that FRBs occur near star formation sites; we need to understand exactly *how near* they are located.

Interestingly, a magnetar-like X-ray burst of 300 ms duration was detected in the direction of the γ-ray binary LSI +61°303 (Torres et al. 2012) (though there is a nonzero probability that the X-ray burst came from an unrelated background magnetar). While the nature of the compact object in LSI +61°303 is still debated, the detection of 269.196 ms radio pulsations from this direction suggests the presence of a neutron star in the binary (Weng et al. 2021). This suggests that the magnetar-versus-binary scenarios are not exclusive. Indeed, the case has been made for magnetars in high-mass X-ray binaries (Popov 2016), superfast X-ray transients (Bozzo et al. 2008), and ultraluminous X-ray sources (Tsygankov et al. 2016).

Thus, the activity period, positional offset, and constraints on local emission are fully consistent with a picture in which FRB 20180916B is a neutron-star HMXB or γ-ray binary system with a late O-type or B-type companion. In such a scenario, interaction between the neutron star's magnetic field and the ionized wind of the companion star may be key to creating the observed radio bursts (FRBs) themselves. Such interactions could create magnetic reconnections that provide the necessary ingredients to produce coherent radio bursts on a wide range of (apparent) timescales and luminosities. The observed periodic activity could then be a reflection of the observer's line of sight. The companion wind will compress the magnetosphere of the neutron star on the companion-facing side and create a tail on the opposite side. An observer may then only see radio bursts when this magnetic tail is pointed toward Earth (Ioka & Zhang 2020). Alternatively, such systems are often found to have very high eccentricity ($e = 0.1$–0.9), and the variable distance between the neutron star and companion could mean that the companion's wind only strongly compresses the neutron star's magnetosphere at certain orbital phases.

Other interacting binary models have also been proposed, including ones in which a stellar companion wind is generated by a millisecond pulsar (Ioka & Zhang 2020), or in which the neutron star's magnetosphere is interacting with orbiting asteroids (Mottez et al. 2020). We cannot exclude such scenarios, since such systems can also satisfy the observed spatial offset. However, such systems could potentially be quite old ($\gtrsim$10–100 Myr), and thus would not naturally explain the relative proximity of FRB 20180916B to such a prominent complex of star formation in the host galaxy.

High-cadence searches for bright radio bursts from Galactic HMXBs and gamma-ray binaries can help to better establish a connection to FRB 20180916B. There are ~90 confirmed and

suspected Be/X-ray binaries and γ-ray binaries and ≈ 131 known HMXBs in the Milky Way and Magellanic Clouds (Reig 2011), at distances of up to 50 kpc. At such distances, these sources would produce bursts of a few hundred MJy ms, if the luminosity is comparable to the weakest bursts seen from FRB 20180916B. Small ($\lesssim 25$ m) radio dishes and individual radio antennas are more than sensitive enough to detect such emission after surmounting the challenge of distinguishing bright astrophysical bursts from radio-frequency interference (Tendulkar et al. 2016).

ORCID iDs

Shriharsh P. Tendulkar ⬤ https://orcid.org/0000-0003-2548-2926
Armando Gil de Paz ⬤ https://orcid.org/0000-0001-6150-2854
Aida Yu. Kirichenko ⬤ https://orcid.org/0000-0002-8139-8414
Jason W. T. Hessels ⬤ https://orcid.org/0000-0003-2317-1446
Mohit Bhardwaj ⬤ https://orcid.org/0000-0002-3615-3514
Cees Bassa ⬤ https://orcid.org/0000-0002-1429-9010
Pragya Chawla ⬤ https://orcid.org/0000-0002-3426-7606
Emmanuel Fonseca ⬤ https://orcid.org/0000-0001-8384-5049
Victoria M. Kaspi ⬤ https://orcid.org/0000-0001-9345-0307
Aard Keimpema ⬤ https://orcid.org/0000-0002-5575-2774
Franz Kirsten ⬤ https://orcid.org/0000-0001-6664-8668
Benito Marcote ⬤ https://orcid.org/0000-0001-9814-2354
Kiyoshi Masui ⬤ https://orcid.org/0000-0002-4279-6946
Kenzie Nimmo ⬤ https://orcid.org/0000-0003-0510-0740
Zsolt Paragi ⬤ https://orcid.org/0000-0002-5195-335X
Mubdi Rahman ⬤ https://orcid.org/0000-0003-1842-6096
Daniel Reverte Payá ⬤ https://orcid.org/0000-0003-0456-149X
Paul Scholz ⬤ https://orcid.org/0000-0002-7374-7119
Ingrid Stairs ⬤ https://orcid.org/0000-0001-9784-8670

References

Apparao, K. M. V., & Tarafdar, S. P. 1997, BASI, 25, 345
Astropy Collaboration, Collaboration, A. M., Price-Whelan, B. M., et al. 2018, AJ, 156, 123
Astropy Collaboration, Robitaille, T. P., Tollerud, E. J., et al. 2013, A&A, 558, A33
Azimlu, M., Marciniak, R., & Barmby, P. 2011, AJ, 142, 139
Bannister, K. W., Deller, A. T., Phillips, C., et al. 2019, Sci, 365, 565
Bassa, C., Tendulkar, S., Adams, E., et al. 2017, ApJL, 843, L8
Beloborodov, A. M. 2017, ApJL, 843, L26
Beniamini, P., & Kumar, P. 2020, MNRAS, 498, 651
Beniamini, P., Wadiasingh, Z., & Metzger, B. D. 2020, MNRAS, 496, 3390
Bhandari, S., Bannister, K. W., Lenc, E., et al. 2020a, ApJL, 901, L20
Bhandari, S., Sadler, E. M., Prochaska, J. X., et al. 2020b, ApJL, 895, L37
Bochenek, C. D., Ravi, V., Belov, K. V., et al. 2020, Natur, 587, 59
Bochenek, C. D., Ravi, V., & Dong, D. 2021, ApJL, 907, L31
Bodaghee, A., Tomsick, J. A., Rodriguez, J., & James, J. B. 2012, ApJ, 744, 108
Bozzo, E., Falanga, M., & Stella, L. 2008, ApJ, 683, 1031
Carrasco, E., Gil de Paz, A., Gallego, J., et al. 2018, Proc. SPIE, 10702, 1070216
Chatterjee, S., Law, C. J., Wharton, R. S., et al. 2017, Natur, 541, 58
CHIME/FRB Collaboration, Amiri, M., Andersen, B. C., et al. 2020a, Natur, 582, 351
CHIME/FRB Collaboration, Amiri, M., Bandura, K., et al. 2019a, Natur, 566, 235
CHIME/FRB Collaboration, Andersen, B. C., Bandura, K., et al. 2019b, ApJL, 885, L24
CHIME/FRB Collaboration, Andersen, B. C., Bandura, K. M., et al. 2020b, Natur, 587, 54
Chittidi, J. S., Simha, S., Mannings, A., et al. 2020, arXiv:2005.13158
Cordes, J. M., & Chatterjee, S. 2019, ARA&A, 57, 417
Cruces, M., Spitler, L. G., Scholz, P., et al. 2021, MNRAS, 500, 448
Cui, X.-H., Zhang, C.-M., Wang, S.-Q., et al. 2021, MNRAS, 500, 3275
Day, C. K., Deller, A. T., Shannon, R. M., et al. 2020, MNRAS, 497, 3335
Ding, H., Deller, A. T., Lower, M. E., et al. 2020, MNRAS, 498, 3736
Dolphin, A. 2016, DOLPHOT: Stellar photometry, Astrophysics Source Code Library, ascl:1608.013
Dubus, G. 2013, A&ARv, 21, 64
Farah, W., Flynn, C., Bailes, M., et al. 2018, MNRAS, 478, 1209
Fich, M., Treffers, R. R., & Dahl, G. P. 1990, AJ, 99, 622
Fonseca, E., Andersen, B. C., Bhardwaj, M., et al. 2020, ApJL, 891, L6
Fujii, M. S., & Portegies Zwart, S. 2011, Sci, 334, 1380

Gaia Collaboration, Brown, A. G. A., Vallenari, A., et al. 2018, A&A, 616, A1
Gaia Collaboration, Prusti, T., de Bruijne, J. H. J., et al. 2016, A&A, 595, A1
Gajjar, V., Siemion, A. P. V., Price, D. C., et al. 2018, ApJ, 863, 2
Gil de Paz, A., Carrasco, E., Gallego, J., et al. 2018, Proc. SPIE, 10702, 1070217
Green, G. M., Schlafly, E., Zucker, C., Speagle, J. S., & Finkbeiner, D. 2019, ApJ, 887, 93
Gutiérrez, L., Beckman, J. E., & Buenrostro, V. 2011, AJ, 141, 113
Harris, C. R., Millman, K. J., van der Walt, S. J., et al. 2020, Natur, 585, 357
Heintz, K. E., Prochaska, J. X., Simha, S., et al. 2020, ApJ, 903, 152
Hessels, J. W. T., Spitler, L. G., Seymour, A. D., et al. 2019, ApJL, 876, L23
Hilmarsson, G. H., Michilli, D., Spitler, L. G., et al. 2020, arXiv:2009.12135
Hobbs, G., Lorimer, D. R., Lyne, A. G., & Kramer, M. 2005, MNRAS, 360, 974
Ioka, K., & Zhang, B. 2020, ApJL, 893, L26
Jedrzejewski, R. I. 1987, MNRAS, 226, 747
Josephy, A., Chawla, P., Fonseca, E., et al. 2019, ApJL, 882, L18
Kaspi, V. M., & Beloborodov, A. M. 2017, ARA&A, 55, 261
Kewley, L. J., Geller, M. J., Jansen, R. A., & Dopita, M. A. 2002, AJ, 124, 3135
Kirsten, F., Snelders, M., Jenkins, M., et al. 2020, NatAs, in press (doi:10. 1038/s41550-020-01246-3)
Kokubo, M., Mitsuda, K., Sugai, H., et al. 2017, ApJ, 844, 95
Levin, Y., Beloborodov, A. M., & Bransgrove, A. 2020, ApJL, 895, L30
Li, C. K., Lin, L., Xiong, S. L., et al. 2020, arXiv:2005.11071
Lorimer, D. R., Bailes, M., McLaughlin, M. A., Narkevic, D. J., & Crawford, F. 2007, Sci, 318, 777
Lu, W., Kumar, P., & Zhang, B. 2020, MNRAS, 498, 1397
Luo, R., Wang, B. J., Men, Y. P., et al. 2020, Natur, 586, 693
Lyutikov, M., Barkov, M. V., & Giannios, D. 2020, ApJL, 893, L39
Macquart, J. P., Prochaska, J. X., McQuinn, M., et al. 2020, Natur, 581, 391
Mannings, A. G., Fong, W.-f., Simha, S., et al. 2020, arXiv:2012.11617
Marcote, B., Nimmo, K., Hessels, J. W. T., et al. 2020, Natur, 577, 190
Marcote, B., Paragi, Z., Hessels, J. W. T., et al. 2017, ApJL, 834, L8
Margalit, B., & Metzger, B. D. 2018, ApJL, 868, L4
Marino, R. A., Rosales-Ortega, F. F., Sánchez, S. F., et al. 2013, A&A, 559, A114
Martins, F., Schaerer, D., & Hillier, D. J. 2005, A&A, 436, 1049
Mereghetti, S., Savchenko, V., Ferrigno, C., et al. 2020, ApJL, 898, L29
Michilli, D., Seymour, A., Hessels, J. W. T., et al. 2018, Natur, 533, 182
Mottez, F., Voisin, G., & Zarka, P. 2020, A&A, 644, A145
Newville, M., Stensitzki, T., Allen, D. B., & Ingargiola, A. 2014, LMFIT: Non-Linear Least-Square Minimization and Curve-Fitting for Python, 0.8.0, Zenodo, doi:10.5281/zenodo.11813
Nimmo, K., Hessels, J. W. T., Keimpema, A., et al. 2020, arXiv:2010.05800
Olausen, S. A., & Kaspi, V. M. 2014, ApJS, 212, 6

Osterbrock, D. E., & Ferland, G. J. 2006, Astrophysics of Gas Nebulae and Active Galactic Nuclei (Mill Valley, CA: Univ. Science Books)
Pascual, S., Cardiel, N., Gil de Paz, A., et al. 2019, in Proc. XIII Scientific Meeting of the Spanish Astronomical Society, Highlights on Spanish Astrophysics X, ed. B. Montesinos et al. (Barcelona: SEA), 227
Pascual, S., Cardiel, N., Picazo-Sanchez, P., Castillo-Morales, A., & Gil de Paz, A. 2018, guaix-ucm/megaradrp: v0.8, Zenodo, doi:10.5281/zenodo.2206856
Pecaut, M. J., & Mamajek, E. E. 2013, ApJS, 208, 9
Petroff, E., Hessels, J. W. T., & Lorimer, D. R. 2019, A&ARv, 27, 4
Platts, E., Weltman, A., Walters, A., et al. 2019, PhR, 821, 1
Pleunis, Z., Michilli, D., Bassa, C. G., et al. 2020, arXiv:2012.08372
Popov, S. B. 2016, A&AT, 29, 183
Popov, S. B. 2020, RNAAS, 4, 98
Prochaska, J. X., Macquart, J.-P., McQuinn, M., et al. 2019, Sci, 366, 231
Rajwade, K. M., Mickaliger, M. B., Stappers, B. W., et al. 2020, MNRAS, 495, 3551
Ravi, V., Catha, M., D'Addario, L., et al. 2019, Natur, 572, 352
Reig, P. 2011, Ap&SS, 332, 1
Ridnaia, A., Svinkin, D., Frederiks, D., et al. 2020, arXiv:2005.11178
Safarzadeh, M., Prochaska, J. X., Heintz, K. E., & Fong, W.-f. 2020, ApJL, 905, L30
Schlafly, E. F., & Finkbeiner, D. P. 2011, ApJ, 737, 103
Scholz, P., Bogdanov, S., Hessels, J. W. T., et al. 2017, ApJ, 846, 80
Scholz, P., Cook, A., Cruces, M., et al. 2020, ApJ, 901, 165
Shannon, R. M., Macquart, J.-P., Bannister, K. W., et al. 2018, Natur, 562, 386
Sob'yanin, D. N. 2020, MNRAS, 497, 1001
Spitler, L. G., Cordes, J. M., Hessels, J. W. T., et al. 2014, ApJ, 790, 101
Spitler, L. G., Scholz, P., Hessels, J. W. T., et al. 2016, Natur, 531, 202
Tavani, M., Casentini, C., Ursi, A., et al. 2020, arXiv:2005.12164
Tendulkar, S. P. 2014, PhD thesis, California Institute of Technology
Tendulkar, S. P., Bassa, C. G., Cordes, J. M., et al. 2017, ApJL, 834, L7
Tendulkar, S. P., Kaspi, V. M., & Patel, C. 2016, ApJ, 827, 59
Torres, D. F., Rea, N., Esposito, P., et al. 2012, ApJ, 744, 106
Tsygankov, S. S., Mushtukov, A. A., Suleimanov, V. F., & Poutanen, J. 2016, MNRAS, 457, 1101
Virtanen, P., Gommers, R., Oliphant, T. E., et al. 2020, NatMe, 17, 261
Walter, R., Lutovinov, A. A., Bozzo, E., & Tsygankov, S. S. 2015, A&ARv, 23, 2
Weng, S.-S., Pan, Z., Qian, L., et al. 2021, ATel, 14297, 1
Worthey, G., & Lee, H.-c 2011, ApJS, 193, 1
Yang, H., & Zou, Y.-C. 2020, ApJL, 893, L31
Zanazzi, J. J., & Lai, D. 2020, ApJL, 892, L15
Zhang, X., & Gao, H. 2020, MNRAS, 498, L1
Zinnecker, H., & Yorke, H. W. 2007, ARA&A, 45, 481